Chemical Geology 697 (2025) 123126

Contents lists available at ScienceDirect

Chemical Geology

journal homepage: www.elsevier.com/locate/chemgeo

Research Paper

Evidence of isotopically heavy carbon in the mantle source beneath Oldoinyo Lengai volcano, Tanzania

A. Sandoval-Velasquez [a,b,*], J. Lages [a], G. Boudoire [b,c], A. Aiuppa [a,b], F.M. Lo Forte [a], L. France [d,e], A.L. Rizzo [f,g]

[a] DiSTeM, Università di Palermo, Via Archirafi 36, 90123 Palermo, Italy
[b] Istituto Nazionale di Geofisica e Vulcanologia (INGV), Sezione di Palermo, Via Ugo La Malfa 153, 90146 Palermo, Italy
[c] Université Clermont Auvergne, CNRS, IRD, OPGC, Laboratoire Magmas et Volcans, F-63000 Clermont-Ferrand, France
[d] Université de Lorraine, CNRS, CRPG, F-54000 Nancy, France
[e] Institut Universitaire de France (IUF), France
[f] Dipartimento di Scienze dell'Ambiente e della Terra, Università di Milano Bicocca, Piazza della Scienza 4, 20126 Milano, Italy
[g] Istituto Nazionale di Geofisica e Vulcanologia (INGV), Sezione di Milano, Via Alfonso Corti 12, 20133 Milano, Italy

ARTICLE INFO

Editor: Don Porcelli

Keywords:
Oldoinyo Lengai
Mantle xenoliths
Fluid inclusions
Mantle metasomatism
Magma degassing
Carbon isotopes

ABSTRACT

Alkali-rich silicate melts and carbonatitic magmas are key to understanding deep carbon cycling, as they may originate from some of Earth's most carbon-rich mantle reservoirs. Determining whether the high carbon contents of these magmas result from low-degree partial melting of depleted or primitive mantle sources or instead require an enriched mantle source metasomatized by recycled, carbon-rich crustal fluids, is critical to elucidating the geodynamic processes that govern deep carbon transport. Carbon isotopes in magmatic and mantle products provide a valuable tool for this purpose. Oldoinyo Lengai (OL) in Tanzania, the only active carbonatitic volcano, has lacked direct carbon isotopic data from fluid inclusions (FIs), which can reveal deep magmatic processes. Here, we present new $\delta^{13}C$ measurements of CO_2 in FIs hosted in OL cumulates and mantle xenoliths. Barometry of secondary FIs in lherzolites indicates entrapment at 510–687 MPa (~19–25 km), suggesting deep fluid trapping or reequilibration during magma ascent or storage. Mantle xenoliths show maximum $\delta^{13}C \approx -2.7$ ‰ (V-PDB), heavier than typical upper mantle values (−4 ‰ to −8 ‰) and comparable to OL fumarole gases. Shallower FIs (22–251 MPa) exhibit lighter $\delta^{13}C$ (−5.0 ‰ to −3.7 ‰). Combined with pressure-dependent $^4He/^{40}Ar^*$ and $CO_2/^3He$ ratios, these data support isotopic fractionation during decompression-driven degassing. An open-system degassing model reconstructs the parental melilititic/Mg-nephelinitic magma's $\delta^{13}C$ at −0.9 ‰, indicating a mantle source metasomatized by crustal carbon. The model also explains OL carbonatites' lighter $\delta^{13}C$ (−6.3 ‰ to −7.8 ‰) as a product of late-stage degassing and shallow crustal liquid immiscibility at 10–12 km depth. Our results shed light on OL's magmatic evolution and deep carbon cycling in sub-continental mantle.

1. Introduction

Continental rift volcanism plays a crucial role in the deep CO_2 cycle, as it enables the remobilization and surface release of large quantities of carbon stored in the subcontinental mantle (Foley and Fischer, 2017; Muirhead et al., 2020). Over geological time, continental rifts may have contributed the most to the volcanic CO_2 budget (Brune et al., 2017), and today they emit some of the CO_2-richest volcanic gases on Earth (Aiuppa et al., 2021). Rift-related magmas and rocks are also notably carbon-rich, including highly alkaline silicate magmas (Foley et al., 2012) such as nephelinites, melilitites, and basanites, and—at the extreme end of the spectrum—carbonatites (Yaxley et al., 2022). Carbonatites, in particular, have been frequently erupted along rifted craton margins throughout the Phanerozoic (Yaxley et al., 2022), and their exceptional carbon enrichment has spurred intense scientific debate, leading to the development of diverse petrogenetic models (Schmidt et al., 2024).

The only active volcano on Earth currently erupting carbonatites is Oldoinyo Lengai (OL) in northern Tanzania, located in the eastern branch of the East African Rift System (Dawson, 1962; Keller and Hoefs, 1995; Koepenick et al., 1996; Teague et al., 2008; Fischer et al., 2009; Barry et al., 2013; Mollex et al., 2018). OL's unique features have

* Corresponding author at: DiSTeM, Università di Palermo, Via Archirafi 36, 90123 Palermo, Italy.
E-mail address: andreslibardo.sandovalvelasquez@unipa.it (A. Sandoval-Velasquez).

https://doi.org/10.1016/j.chemgeo.2025.123126
Received 30 July 2025; Received in revised form 25 October 2025; Accepted 31 October 2025
Available online 2 November 2025

prompted numerous studies aimed at deciphering the origin and evolution of its magmatic system (Peterson, 1989; Dawson et al., 1995; Bell and Keller, 1995; Koepenick et al., 1996; Teague et al., 2008; Fischer et al., 2009; Barry et al., 2013; De Moor et al., 2013; Mollex et al., 2018; Casola et al., 2020). Recent petrological and geochemical evidence suggests that OL carbonatites likely form via low-pressure differentiation of mantle-derived, melilite- or olivine-rich melilititic nephelinite magmas generated by low-degree mantle melting (1–5 %) (Peterson, 1989; Kjarsgaard et al., 1995; Fischer et al., 2009; Mourey et al., 2023).

The peculiar nature of OL volcanism has also motivated efforts to characterize its mantle source using isotopic tracers. Radiogenic isotope analyses (Nd, Sr, and Pb) of OL volcanic products indicate a complex mantle source, incorporating both HIMU (High-μ) and EM1 (Enriched Mantle 1) components (Bell and Dawson, 1995). Helium isotope data from summit fumaroles and fluid inclusions (FIs) in lavas and xenoliths (Teague et al., 2008; Fischer et al., 2009; Mollex et al., 2018) range from 4 to 7 Ra (where Ra is the atmospheric $^3He/^4He$ ratio), consistent with a Subcontinental Lithospheric Mantle (SCLM) origin (6.1 ± 0.9 Ra; Gautheron and Moreira, 2002). However, Hilton et al. (2011) and Barry et al. (2013) suggested additional contributions from two other mantle endmembers—MORB-type (8 ± 1 Ra) and a plume-like component ($^3He/^4He$ = 9–15 Ra)—to explain the isotopic signatures observed in lavas, tephra, bubbling mud pools, and hydrothermal springs in the nearby Rungwe Volcanic Province (RVP) of southern Tanzania.

Regarding carbon isotopes, available data come primarily from OL volcanic gases, which show relatively homogeneous $\delta^{13}C$ values between −4.0 ‰ and − 2.4 ‰ (Fischer et al., 2009), and from fresh natrocarbonatite lavas with values ranging from −6.3 ‰ to −7.8 ‰ (Keller and Hoefs, 1995; Fischer et al., 2009). However, because carbon isotopes can undergo significant fractionation during magmatic degassing (Javoy et al., 1989; Mattey, 1991; Deines, 2002; Aubaud, 2022), neither gas emissions nor bulk lava compositions may reliably reflect the mantle source $\delta^{13}C$—especially if natrocarbonatites form via shallow-level immiscibility. As shown by Frezzotti et al. (2002b), mantle xenoliths offer a more robust archive, as they can trap CO_2-rich fluids at source within mineral-hosted FIs (Pearson et al., 2014). Indeed, in both continental rift (Rizzo et al., 2018; Sandoval-Velasquez et al., 2021a; Halldórsson et al., 2022) and ocean island settings (Lo Forte et al., 2024; Sandoval-Velasquez et al., 2024), mantle xenoliths have proven essential for identifying carbon-rich fluid components likely derived from the recycling of crustal material into the mantle.

Since such data are currently lacking for OL, key questions remain unanswered: does the carbon-rich nature of OL magmas reflect (i) low-degree partial melting of a typical mantle source with upper mantle-like $\delta^{13}C$ (−4 ‰ to −8 ‰; Sano and Marty, 1995), (ii) melting of a carbon-enriched mantle reservoir containing recycled crustal carbon, or (iii) subsequent isotopic fractionation due to decompression-driven degassing and immiscibility of parental melts?

To address these questions, we present new $\delta^{13}C$ data for CO_2 contained in FIs hosted in cumulates (ijolites and wehrlites) and mantle xenoliths (harzburgites and lherzolites) collected in OL-related alkaline- and ultramafic lavas. These data are integrated with light noble gas isotopic compositions, mineral chemistry, and FIs barometry to constrain the carbon isotopic composition of the mantle source beneath OL and to shed light on the genesis of this unique active carbonatitic system.

2. Materials and methods

2.1. Samples description

Xenoliths were collected from monogenetic craters located both around the flanks and at the summit of Oldoinyo Lengai (OL) volcano (Fig. 1 and Table S1). The suite of samples includes both cumulates and mantle xenoliths, with compositions ranging from ijolites and wehrlites to harzburgites and lherzolites. The petrography of xenoliths 10TL01, 10TL05, 14TG21, and 14TG22 is described in Mollex et al. (2018) and Mourey et al. (2023). Xenoliths 10TL01 and 10TL05 were collected from the rim of the northeast crater formed during the 2007 explosive eruption at OL. These are classified as shallow cumulates (ijolites) composed mainly of nepheline, clinopyroxene, and garnet, with subordinate phases including apatite, sulfides, Ti-magnetite, wollastonite, and quenched melt (Mollex et al., 2018). In contrast, xenoliths 14TG21 and 14TG22 were sampled from the northernmost portion of the phlogopite- and olivine-bearing melilitite tuffs, dated to 353 ± 65 ka (Sherrod et al., 2013), and are classified as wehrlite. Their mineral assemblage—comprising spinel, olivine, clinopyroxene, phlogopite, pargasite, and subordinate sulfides—is indicative of deep crustal crystallization (Mourey et al., 2023).

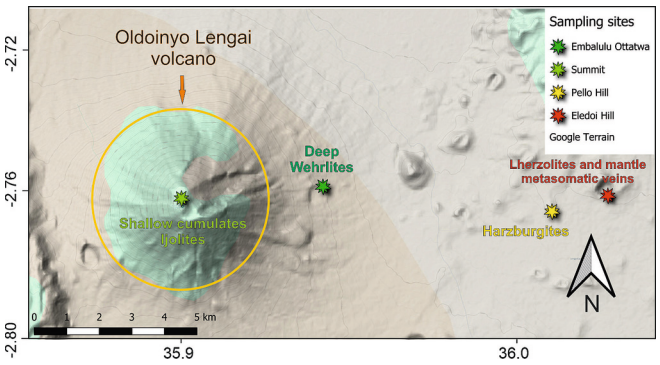

Fig. 1. Map showing the sampling localities of the crustal and mantle xenoliths. Coordinates are reported in Table S1. Image from Google April 2025.

The remaining xenoliths, classified as lherzolites and harzburgites, exhibit a typical upper mantle mineralogy. Xenoliths 14TG19G and 14TG11D are harzburgites composed mainly of olivine and orthopyroxene, and are interpreted as representative of a refractory mantle source. The lherzolites are represented by samples 14TG24-C9a, 14TG24B-3, and 14TG12c-a, mainly distinguished by the presence of Cr-rich clinopyroxenes. Samples 14TG24-C9b and 14TG12c-b are mantle metasomatic veins consisting mainly of Cr-poor clinopyroxene with abundant phlogopite and ilmenite.

Barometric estimates from CO_2-densimetry of FIs based on Raman spectroscopy and mineral chemistry were conducted on most of the xenoliths and are reported in Tables S2 and S3. Further details on the analytical procedures are provided in the supplementary information.

2.2. Noble gas and CO_2 isotopes

For elemental and isotopic measurements of noble gases (He–Ne–Ar), all samples were crushed and sieved to allow hand-picking of olivine, clinopyroxene, and phlogopite crystals with diameters >0.5 mm. For each aliquot, between 0.2 g (minimum) and 1 g (maximum) of crystals was collected. After selection, the samples were ultrasonically cleaned using HNO_3, deionized water, and high-purity acetone. The cleaned samples were then accurately weighed and loaded into an ultra-high-vacuum (UHV) crusher for noble gas analysis. The crusher system was evacuated and baked at 120 °C for 48 h. Once UHV conditions were achieved, FIs gases were released by single-step crushing at approximately 200 bar and room temperature (21 °C). The total amount of CO_2 released was quantified by measuring the total pressure of the gas mixture ($CO_2 + N_2 + O_2$ + noble gases) using an IONIVAC Transmitters ITR90 pressure gauge within a known system volume. To isolate the CO_2 component, the residual pressure from $N_2 + O_2$ + noble gases was measured after CO_2 was cryogenically removed using a “cold finger” immersed in liquid nitrogen. For noble gas analysis, the residual gas mixture was purified using Zr—Al getter pumps within a UHV stainless-steel preparation line. Subsequently, Ar (as well as Kr and Xe, if present) was cryogenically removed using an active charcoal “cold finger”

immersed in liquid nitrogen. He and Ne were sequentially adsorbed onto a cold head with active charcoal cooled to 10 K and then stepwise heated to 40 K and 80 K to release He and Ne, respectively.

He and Ne isotopes were analyzed using two split-flight-tube mass spectrometers (Helix SFT, Thermo), while Ar isotopes were analyzed using a multi-collector mass spectrometer (Argus, GVI). Analytical uncertainties (1σ) for the measured isotope ratios were as follows: <2.7 % for $^{3}He/^{4}He$, <6.3 % for $^{20}Ne/^{22}Ne$, <7.5 % for $^{21}Ne/^{22}Ne$, <2.0 % for $^{40}Ar/^{36}Ar$, and < 1.7 % for $^{38}Ar/^{36}Ar$. The $^{20}Ne/^{22}Ne$ and $^{21}Ne/^{22}Ne$ ratios were corrected for isobaric interferences at m/z 20 ($^{40}Ar^{2+}$) and m/z 22 ($^{44}CO_2^{2+}$), respectively. The $^{3}He/^{4}He$ ratio was further corrected for atmospheric contamination based on the measured $^{4}He/^{20}Ne$ ratio, as follows:

$$Rc/Ra = \left((R_M/Ra)(He/Ne)_M - (He/Ne)_A\right) / \left((He/Ne)_M - (He/Ne)_A\right) \quad (1)$$

where subscripts M and A refer to measured and atmospheric theoretical values, respectively (air has $^{4}He/^{20}Ne = 0.318$). The corrected $^{3}He/^{4}He$ ratios are reported as Rc/Ra values.

^{40}Ar was corrected for air contamination ($^{40}Ar^{*}$) assuming that the measured ^{36}Ar has an atmospheric origin as follows:

$$^{40}Ar^{*} = {}^{40}Ar_{sample} - \left[{}^{36}Ar_{sample} \times \left({}^{40}Ar/{}^{36}Ar\right)_{air}\right] \quad (2)$$

$$^{40}Ar_{air} = {}^{40}Ar_{sample} - {}^{40}Ar \quad (3)$$

From samples 14TG12c-b, 14TG24-C9b, 10TL05, and 14TG21, CO_2 was extracted from FIs hosted in clinopyroxene, and both the CO_2 concentration and the $^{13}C/^{12}C$ ratio were determined. The carbon isotope composition is expressed using delta notation ($\delta^{13}C$), in parts per thousand (‰), relative to the V-PDB international standard. $\delta^{13}C$ measurements were performed exclusively on clinopyroxenes, as this was the only mineral phase in which FIs contained sufficient CO_2 for isotopic analysis. To this end, between 0.35 g and 0.64 g of fresh clinopyroxene crystals, with diameters ≥0.5 mm, were hand-picked from fragmented xenoliths. The crystals were cleaned using an ultrasonic bath in 10 % HCl, followed by deionized water, then dried, weighed, and loaded into a crusher system consisting of a stainless-steel sample holder and a hydraulic press capable of exerting a single-step pressure of approximately 200 bar. During mechanical crushing for CO_2 extraction and carbon isotope analysis, a glass sampler submerged in liquid nitrogen was used to trap the released CO_2 by freezing. A vacuum pump maintained system pressure 10^{-3} mbar. The glass sampler was subsequently connected to a glass line equipped with a 626B Baratron® Absolute Capacitance Manometer (MKS; measuring range: 10^{-3} to 10 mbar) for CO_2 purification and quantification (expressed in mol/g). The purified CO_2 was condensed in the same sampler, which was then brought to atmospheric pressure by adding high-purity helium and transferred to the stable isotope laboratory for isotopic analysis.

The $^{13}C/^{12}C$ ratio was determined using a Thermo (Finnigan) Delta Plus XP continuous-flow isotope ratio mass spectrometer (CF-IRMS), coupled with a Trace GC gas chromatograph and a Thermo (Finnigan) GC/C III interface. The analytical uncertainty for $\delta^{13}C$ was better than ±0.4 ‰ (2σ). The isotopic analyses of both noble gases and CO_2 were conducted at the laboratories of INGV, Sezione di Palermo (Italy). Further details regarding the sample preparation and analytical protocols can be found in Gennaro et al. (2017), Rizzo et al. (2018) and Sandoval-Velasquez et al. (2021a).

3. Results

3.1. FIs entrapment pressures

Orthopyroxene and clinopyroxene crystals, in most of the samples, display numerous trails of secondary FIs (Roedder, 1984) developed along healed crystal fractures (Fig. S1). An exception is observed in sample 10TL01, where FIs are isolated supporting their interpretation as primary in origin (Fig. S1A). Stretching and necking down patterns are observed in samples 14TG19G and 14TG21 (Fig. S1) suggesting reequilibration of part of the FIs. In general, CO_2 density in FIs clinopyroxene and orthopyroxene crystals from the shallow cumulates (10TL01, 10TL05; Fig. S1A), the deep cumulates (14TG21 and 14TG22; Fig. S1B), and the mantle xenoliths (14TG19G, 14TG11D; 14TG24-C9a, 14TG12c-a; 14TG24-C9b, 14TG12c-b; 14TG24B-3; Fig. S1 C-E), ranges from 0.08 to 0.95 g/cc (0.08 to 0.98 g/cc by adding 10 mol% of H_2O). Barometric estimations indicate a wide range of variability between 29 and 687 MPa (Fig. 2 and Table S2); corresponding depths were estimated using the lithostatic pressure formula and a crustal density of 2.750 g/cm^3 (Christensen and Mooney, 1995). In detail, **(i)** coarse-grained shallow cumulates exhibit the shallowest pressures with values from 0 to 4 km (33–101 MPa); **(ii)** lower crust cumulates xenoliths show two data groups: the shallowest between 1 and 10 km (39–261 MPa) and the deepest about 19 km (~498 MPa); while **(iii)** mantle xenoliths, although exhibiting considerable variability, record the maximum depths at OL (18 - 25 km; 490–670 MPa).

3.2. Mineral chemistry

Mineral chemistry data is presented in Table S3. Clinopyroxenes from ijolites (samples 10TL01 and 10TL05) are characterized by Mg# <80 and low Al_2O_3 contents (<1.5 wt%), features that clearly distinguish them from clinopyroxenes found in deep cumulates and mantle xenoliths (Mg# of 83–97; Fig. 3A – B). Ti/Al ratios reflect systematic differences between crustal cumulates and mantle xenoliths: elevated Ti/Al values (0.22–0.55) are observed in clinopyroxenes from wehrlites and some ijolites, in contrast to the lower ratios of lherzolites (0.05–0.35). In all samples, clinopyroxene exhibits negligible core-to-rim variations in Mg#, Ti/Al ratios, and CaO contents. Systematic differences are evident in olivine compositions, particularly in forsterite (Fo) and NiO contents (Fig. 3C). Olivines from wehrlites (interpreted as deep cumulates) display Fo_{80-82}, whereas higher forsterite contents are recorded in mantle xenoliths: Fo_{84-93} in lherzolites and Fo_{92-94} in harzburgites. Olivines from wehrlites are characterized by the lowest NiO

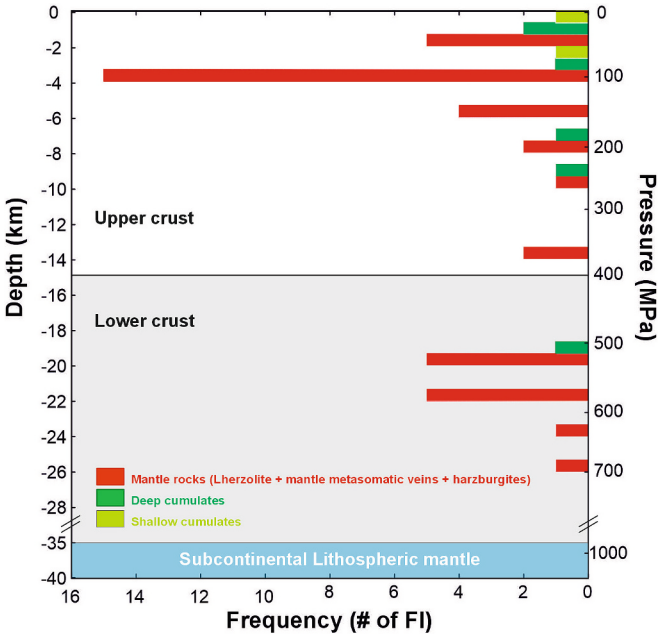

Fig. 2. Histogram showing the distribution of FIs trapping pressures measured in OL xenoliths presented in this work and from the literature (Table S2). The depths relative to the local lower crust and the SCLM were designed after Roecker et al. (2017), Plasman et al. (2017) and Daud et al. (2023).

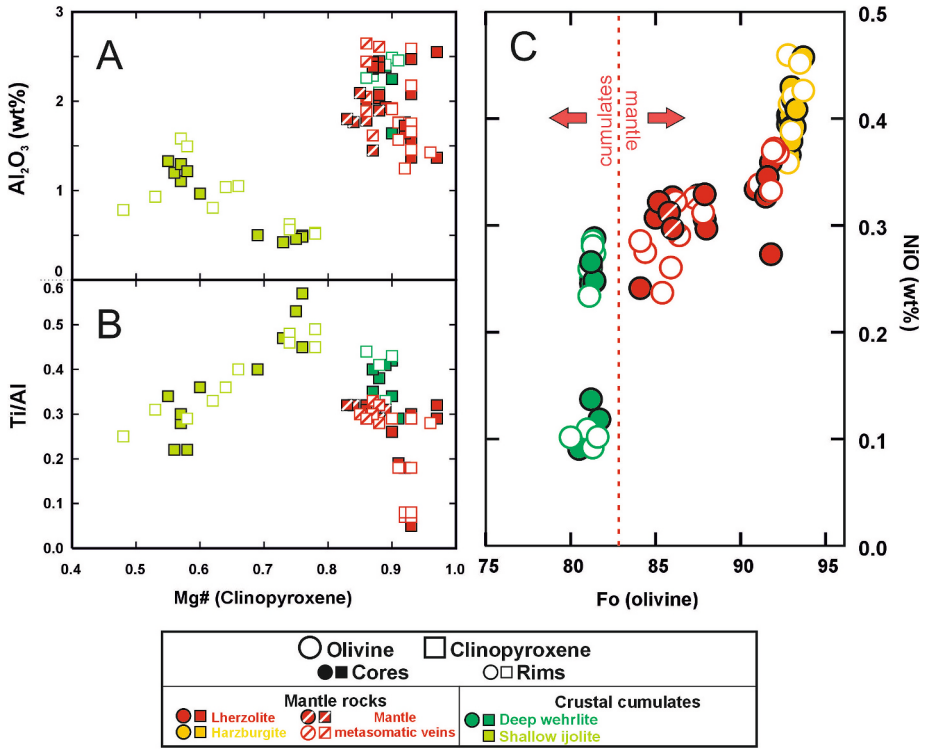

Fig. 3. Mg# vs A) Al_2O_3 and B) Ti/Al in clinopyroxenes. C) Fo vs NiO in olivines; the dotted red line emphasizes the difference in Fo between cumulates and mantle xenoliths. (For interpretation of the references to colour in this figure legend, the reader is referred to the web version of this article.)

contents (<1.5 wt%) and the highest CaO concentrations (>0.30 wt%), whereas olivines from mantle xenoliths exhibit elevated NiO contents (up to 0.46 wt%) and markedly lower CaO levels (0.11–0.01 wt%). Similar to clinopyroxenes, individual olivine grains from both cumulates and mantle xenoliths display minimal core-to-rim compositional zoning.

3.3. CO_2 and noble gas isotopic data

CO_2 is the most abundant volatile species in all OL FIs (Fig. S1F), particularly in those hosted within clinopyroxene, where concentrations reach up to 6.9×10^{-7} mol/g (Table 1). Note that fluid inclusions analysis by Raman spectroscopy revealed that most of the fluid inclusions entrapped in olivine crystals from the harzburgites (samples 14TG19G and 14TG11D) and from the deep cumulates (14TG21 and 14TG22) has no detectable CO_2 but contain carbonates. It suggests for these samples a predominant process of carbonate-forming from initial entrapped CO_2. This hypothesis is confirmed by the unusual low Total Gas Content (TGC) and CO_2 content released by crystal crushing of these products (see Fig. S2 where these samples diverge from the classical positive correlation between entrapment depth and CO_2-TGC; Boudoire et al., 2018). $CO_2/^3He$ ratios range from 2.5×10^8 to 1.9×10^9, while corresponding $\delta^{13}C$ values vary from −5 ‰ to −2.7 ‰. On average, ^4He contents are 1.0×10^{-11}, 3.9×10^{-11}, and 1.1×10^{-12} mol/g in olivine, clinopyroxene, and phlogopite, respectively (Table 1). The analyzed aliquots display $^4He/^{40}Ar^*$ ratios ranging from 0.2 to 3.7 in olivine and from 0.6 to 13.5 in clinopyroxene, indicating a magmatic origin for the FIs (Fig. S3). The presence of a minor atmospheric component in the inclusions is evidenced by relatively low $^4He/^{20}Ne$ and $^{40}Ar/^{36}Ar$ ratios (reaching up to 1902 and 4150, respectively; Fig. S4).

Rc/Ra values ($^3He/^4He$ ratios corrected for atmospheric contamination) are relatively homogeneous across the three analyzed mineral phases, ranging from 5.6 to 7.4 Ra (Table 1). Notably, phlogopite crystals exhibit the highest values in the dataset, from 7.2 to 7.4 Ra. Samples suspected of being affected by secondary processes, such as helium loss, cosmogenic ^3He or radiogenic ^4He addition were excluded from the final interpretation (see supplementary information for more details). The filtered dataset yields average Rc/Ra values of 6.6 ± 0.4 Ra for mantle xenoliths and 6.2 ± 0.5 Ra for crustal cumulates. These results are consistent with previous measurements from OL summit fumaroles and xenoliths (e.g., Teague et al., 2008; Fischer et al., 2009; Mollex et al., 2018), and overlap the lower end of both the MORB and SCLM ranges (8 ± 1 Ra and 6.1 ± 0.9 Ra, respectively; Graham, 2002; Gautheron and Moreira, 2002).

Together, these findings suggest the existence of a relatively homogeneous isotopic signature within the magmatic plumbing system beneath OL. This signature appears unaffected by significant crustal assimilation during magma ascent and likely reflects the isotopic characteristics of the local subcontinental mantle.

4. Discussion

4.1. Regions of the OL plumbing system sampled by our xenoliths

The geometry of the OL system has been reconstructed through the inversion of ground deformation data, seismic records, and petrological observations (Roecker et al., 2017; Reiss et al., 2021, 2022; Daud et al., 2023). It has been proposed that the shallowest part of the plumbing system consists of two magma ponding zones located between 1 and 3 km depth (Daud et al., 2023). These shallow reservoirs are connected to a sill complex located in the mid-crust (at ~8–12 km depth), which is in turn fed—through a complex network of dykes—by a deep reservoir situated at 18–25 km depth in the lower crust (Roecker et al., 2017; Daud et al., 2023). Based on their tomographic model, Roecker et al. (2017) also proposed the existence of an even deeper magma storage zone at the boundary between the lower crust and the upper mantle, at approximately 35–50 km depth. This deeper reservoir is thought to feed not only the OL plumbing system, but also the volcanic activity of the Natron Basin and the Gelai monogenetic field. Petrological studies of lavas and deep crustal cumulates also support the existence of a deep crustal reservoir (~25–35 km) that regularly recharges a mid-crustal

Table 1
The isotopic composition of CO_2 and noble gas in fluid inclusions fom OL xenoliths.

Sample	Rock	Mineral	CO2[a]	δ13C	CO2 /3He[a]	4He	3He	CO2[b]	40Ar	36Ar	40Ar*[d]	4He/ 20Ne	4He/ 40Ar*	R/ Ra	Rc/ Ra[c]	error (+/−)	40Ar/ 36Ar	error (+/−)	CO2/ 3He[b]	TGC	3He/ 36Ar
11D	Harzburgite	Ol	–	–	–	5,11E-13	4,82E-18	2,53E-09	1,48E-11	4,58E-14	1,26E-12	13,2	0,41	6,79	6,90	0,09	326,3	0,5	5,24E+08	5,99E-09	0,0001
11D (replicate)	Harzburgite	Ol	–	–	–	1,15E-13	9,16E-19	5,09E-10	5,18E-12	1,56E-14	5,72E-13	8,3	0,20	5,71	5,90	0,10	335,9	0,2	5,56E+08	2,30E-09	0,0001
19G	Harzburgite	Ol	–	–	–	6,33E-12	5,59E-17	2,18E-08	6,15E-12	3,03E-15	5,26E-12	672,7	1,20	6,35	6,30	0,06	2050,1	1,4	3,91E+08	2,21E-08	0,0184
24B-3	Lherzolite	Ol	–	–	–	3,07E-11	2,81E-16	5,82E-10	1,53E-11	1,67E-14	1,04E-11	1296,6	2,95	6,61	6,60	0,06	924,3	2,9	2,07E+06	1,30E-09	0,0169
12C-a	Lherzolite	Ol	–	–	–	5,37E-12	4,84E-17	3,98E-10	3,45E-12	2,02E-15	2,85E-12	1902,0	1,89	6,49	6,50	0,07	1721,6	1,5	8,23E+06	4,97E-10	0,0239
14TG24-C9a	Lherzolite	Ol	–	–	–	7,82E-12	7,14E-17	7,51E-10	4,45E-12	7,95E-15	2,11E-12	693,6	3,71	6,57	6,60	0,06	566,7	0,3	1,05E+07	1,09E-09	0,0090
		Cpx	–	–	–	1,74E-11	1,56E-16	1,18E-07	8,59E-12	5,95E-15	6,83E-12	1401,7	2,55	6,45	6,50	0,06	1458,4	1,2	7,57E+08	1,20E-07	0,0262
14TG24-C9b	Metasomatic vein	Ol	–	–	–	6,44E-12	6,02E-17	5,56E-10	8,53E-12	2,21E-14	2,01E-12	188,1	3,21	6,73	6,70	0,07	390	1,8	9,24E+06	1,80E-09	0,0027
		Cpx	4,62E-07	-5,00	1,24E+09	4,11E-11	3,71E-16	3,51E-07	4,77E-11	1,01E-13	1,80E-11	297,8	2,29	6,5	6,50	0,06	478,7	0,4	9,46E+08	3,56E-07	0,0037
		Phlog	–	–	–	1,67E-12	1,67E-17	1,22E-08	8,18E-12	2,56E-14	6,11E-13	50,1	2,73	7,14	7,20	0,07	322,8	0,2	7,30E+08	–	0,0007
12c-b	Metasomatic vein	Cpx	8,40E-07	-2,65	1,81E+09	5,27E-11	4,65E-16	6,88E-07	7,47E-11	4,63E-14	6,11E-11	899,4	0,86	6,34	6,30	0,06	1627,2	2,8	1,48E+09	6,92E-07	0,0100
		Phlog	–	–	–	4,77E-13	4,79E-18	3,2E-09	1,34E-11	4,15E-14	1,1E-12	8,7	0,43	7,18	7,40	0,11	325,5	0,2	6,68E+08	–	0,0001
14TG21	Wehrlite	Ol	–	–	–	1,39E-11	1,12E-16	6,09E-10	1,37E-10	3,33E-14	1,27E-10	299,1	0,11	5,77	5,80	0,05	4150,3	7,9	5,46E+06	1,68E-09	0,0034
		Cpx	8,36E-08	-4,07	1,87E+09	8,47E-12	7,8E-17	1,45E-07	2,91E-11	5,02E-14	1,42E-11	118,2	0,60	6,58	6,60	0,06	581,5	2,7	1,87E+09	1,47E-07	0,0016
14TG-22b	Wehrlite	Ol	–	–	–	2,05E-11	1,61E-16	4,28E-10	2,97E-11	1,07E-14	2,65E-11	1367,9	0,77	5,64	5,60	0,06	2784	18,1	2,65E+06	1,10E-09	0,0152
10TL01	Ijolite	Cpx	–	–	–	1,59E-11	1,37E-16	1,07E-08	2,20E-11	6,88E-14	1,64E-12	157,3	9,74	6,19	6,20	0,06	322,7	0,4	7,82E+07	1,29E-08	0,0020
10TL05	Ijolite	Cpx	1,27E-07	-3,69	2,52E+08	1,01E-10	9,89E-16	2,50E-07	2,07E-11	4,47E-14	7,49E-12	1433,8	13,51	6,98	7,00	0,06	466,7	0,8	2,52E+08	2,52E-07	0,0221

Gas and total gas contents (TGC) are expressed in mol/g; uncertainties are 1σ.

[a] CO_2 and $CO_2/^3He$ measured from the glass line

[b] Estimation of CO_2 and $CO_2/^3He$ during noble gases analysis;

[c] $\mathbf{Rc/Ra = R_m/Ra * (He/Ne_{(m)} - He/Ne_{(a)})/(He/Ne_{(m)} - He/Ne_{(a)})}$; R_m/Ra and $He/Ne_{(m)}$ are the measured values, $He/Ne_{(a)}$ is the atmospheric value of 0,318 (Ozima and Podosek, 2001)

[d] $\mathbf{^{40}Ar^* = {}^{40}Ar_{(m)} - ({}^{36}Ar_{(m)} * ({}^{40}Ar/{}^{36}Ar_{(a)}))}$; $^{40}Ar_{(m)}$ and $^{36}Ar_{(m)}$ are the measured values and $^{40}Ar/^{36}Ar_{(a)}$ is the atmospheric value = 295,5 (Ozima and Podosek, 2001)

one (~8–15 km) where phonolites and carbonatites coexist (Mourey et al., 2023).

We use our mineral chemistry and barometric results to constrain the spatial position of our samples within specific sub-regions of the plumbing system described above. For example, Ti/Al ratios in clinopyroxene (cpx) crystals show systematic differences between cumulates and mantle xenoliths, which can be interpreted as indicative of different provenance depths within the OL system. In ijolites and wehrlites (samples 14TG21, 14TG − 22-B, and 10TL01), Ti/Al ratios in cpx are typically >0.35, while in mantle xenoliths they are generally <0.35. Higher Ti/Al ratios are typically interpreted as indicating lower crystallization pressures (e.g., Boudoire et al., 2019; Lo Forte et al., 2024), and in our case support a shallower origin for cumulates. This interpretation is corroborated by our barometric estimated in FIs shown in Fig. 2, where most of the data fall into three sub-groups that broadly correspond to the main storage regions of the previously described magmatic system. The first group corresponds to depths between 0 and 6 km (< 140 MPa), the second to 8–10 km (225–265 MPa), and the third to 18–25 km (480–687 MPa). Depths <10 km are mostly associated with cumulates, while depths >19 km are found only in samples 14TG12c-a, 14TG19G and 14TG12c-b (the latter with an estimated $\delta^{13}C$ of −2.7 ‰) which are classified as mantle xenoliths of lherzolitic or harzburgitic composition and fall within the depth interval proposed for the deep magma storage zone by Roecker et al. (2017).

4.2. Carbon isotopes in xenoliths, and inferences into the isotopic signature of OL parental melts

FIs in cumulates and mantle xenoliths exhibit $\delta^{13}C$ values ranging from −5.0 ‰ to −2.7 ‰, thus falling within the range reported for OL volcanic gases and fresh carbonatitic lavas (−7.8 ‰ to −2.4 ‰; Keller and Hoefs, 1995; Fischer et al., 2009; Barry et al., 2013). Notably, the heaviest $\delta^{13}C$ values for both FIs and volcanic gases (−2.7 ‰ and − 2.4 ‰, respectively; this study and Fischer et al., 2009) lie well outside the typical $\delta^{13}C$ range for MORB mantle carbon (Sano and Marty, 1995). This becomes particularly significant when considering that the heaviest $\delta^{13}C$ value (−2.7 ‰) is associated with FIs in sample 14TG12c-b, which also corresponds to one of the highest estimated entrapment pressures (617 MPa; Fig. 4A).

The $^4He/^{40}Ar^*$ ratio (and to a lesser extent, CO_2 concentrations; Fig. S2) also shows a systematic correlation with estimated FIs pressures (Fig. 4B), increasing from approximately 0.86 at 23 km depth to 9.74 at 4 km. Because $^4He/^{40}Ar^*$ is known to increase during magmatic degassing due to the ~7–10 times greater solubility of He compared to Ar in silicate melts (Fischer et al., 2005; Iacono-Marziano et al., 2010), the observed pressure-dependent variations in Fig. 4A–B suggest that the FIs population records different stages of decompression-driven degassing. Each sample of FIs thus likely represents a specific degassing step along the OL magma's ascent path.

This is particularly relevant because, during magmatic degassing, heavy carbon (^{13}C) is preferentially partitioned into the CO_2-rich fluid phase relative to the coexisting melt (Javoy et al., 1989; Deines, 2002; Aubaud, 2022), leaving the residual melt and late-formed gas progressively enriched in ^{12}C and thus displaying more negative $\delta^{13}C$ values. If the extent of degassing significantly controls the isotopic and chemical composition of FIs (as shown in Fig. 4A–B), then the measured $\delta^{13}C$ values of FIs may underestimate the original carbon isotopic composition of the parental OL melt and its mantle source. Our FIs data in Fig. 4A–B provide an opportunity to construct a pressure-dependent model of magmatic degassing in order to back-calculate the primary $\delta^{13}C$ signature of the magma source. For this, we apply the Fractional Equilibrium Degassing (FED) equations developed by Macpherson and Mattey (1994), which have previously been used in similar contexts by Boudoire et al. (2018) and Lo Forte et al. (2024) to interpret FIs data from La Réunion Island and Fogo volcano, respectively:

$$\delta^{13}C_m = \delta^{13}C_{m,i} + (\Delta^* lnF) \quad (4)$$

$$\delta^{13}C_v = \delta^{13}C_m + \Delta \quad (5)$$

where $\delta^{13}C_m$, $\delta^{13}C_v$ are the $\delta^{13}C$ signatures of the melt and the vapor, respectively, at each step of the degassing; $\delta^{13}C_{m,i}$ is the signature of the starting melt and Δ is the $^{13}C/^{12}C$ vapor-melt enrichment factor assumed equal to +2.74 ‰ (Mattey, 1991; Boudoire et al., 2018; Lo Forte et al., 2024).

Use of Eq. (4) requires that the residual fraction (F) of CO_2 remaining in the melt at each degassing step or pressure be parameterized. This, in

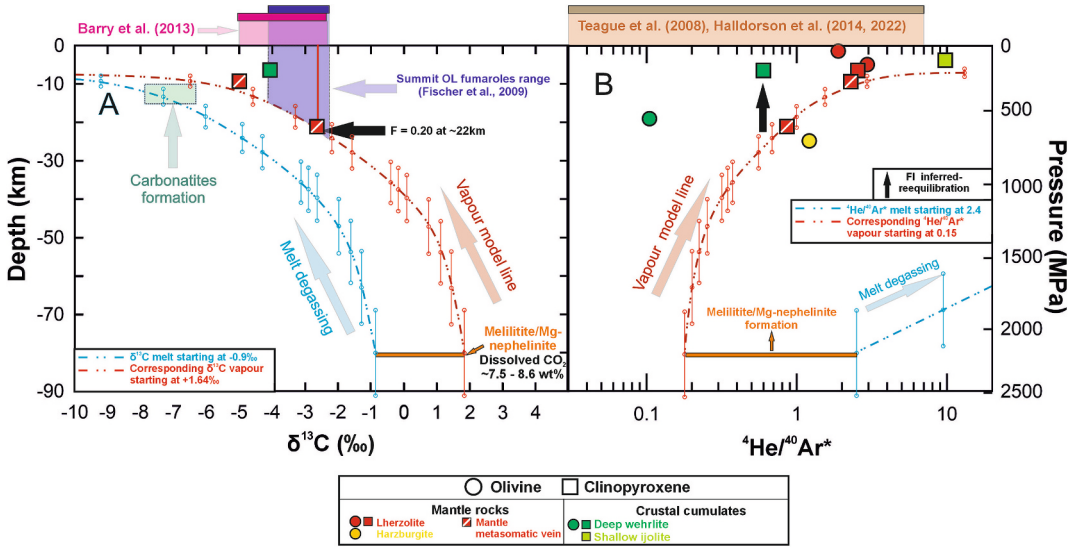

Fig. 4. Open-system degassing modelling for A) $\delta^{13}C$ and B) $^4He/^{40}Ar^*$ based on FIs barometric data. Modelling is based on the equations proposed by Macpherson and Mattey (1994), see main text for details. The red and blue vertical lines represent the uncertainty of the model based on the pressure estimations of FIs (~ 15 %; see supplementary material for further details). Melilitite/Mg-nephelinite formation was set at 80 km depth based on the information provided in Mattey et al. (2013), Ebinger et al. (1997) and the modelled $\delta^{13}C$ and $^4He/^{40}Ar^*$ratios. Carbonatite formation ranges are proposed between 10 and 12 km depth. Purple, violet and orange fields on the upper part of the diagrams represent the variability of $\delta^{13}C$ and $^4He/^{40}Ar^*$ data for gases and FIs from OL and the neighboring Rungwe Volcanic Province (RVP) reported in the literature. (For interpretation of the references to colour in this figure legend, the reader is referred to the web version of this article.)

turn, necessitates knowledge of the original CO_2 content in the primary (parental), undegassed melt. Based on recent experimental petrological composition of the host magma that transported the deep cumulates (samples 14TG21 and 14TG22; Mourey et al., 2023) to the surface—and considering that most mantle xenoliths found in the vicinity of OL are hosted in melilitites (Mattsson et al., 2013)—we assume that parental OL magmas to be melilititic to Mg-nephelinitic in composition and adopt these as the starting melts in our model. Melilititic and Mg-nephelinitic magmas are the most primitive erupted at OL and are believed to originate at ~60–90 km depth, near the base of the local SCLM (Ebinger et al., 1997; Mattsson et al., 2013). Following Keller et al. (2006) and Mourey et al. (2023), we consider melilitites and Mg-nephelinites as the best candidates for primary melt compositions in the OL area, due to their compositional affinities and their high Mg# and elevated Ni and Cr contents.

Using the CO_2 solubility model of Eguchi and Dasgupta (2018), we estimate that a typical OL melilititic or Mg-nephelinitic magma (see Table 2 for initial magma compositions), formed at 2.2GPa (~75–80 km depth) under an oxygen fugacity of 2 log units above the Quartz–Fayalite–Magnetite (QFM) buffer and at a temperature of 1200 °C (Keller et al., 2006; Mattsson et al., 2013; Mourey et al., 2023), can hold up from 7.5 wt% (Mg-nephelinitic magma) to 8.6 wt% (melilititic magma) dissolved CO_2 at saturation (solubility constant $S_{CO2} = 7.88 \times 10^{-8}$ mol/g/bar). We consider this range (7.5–8.6 wt%) for the parental melt to be realistic and the most probable, as it is consistent with the maximum CO_2 contents found in melt inclusions trapped in silicate glasses from the 2007–2008 eruption at OL (8.7 wt%; De Moor et al., 2013). Using this parental melt CO_2 contents, we apply Eqs. (4) and (5) to back-calculate the initial $\delta^{13}C_m$ of the melt required to reproduce the $\delta^{13}C$ values measured in FIs from mantle metasomatic xenoliths (Fig. 4A). The best fit between the model vapor curve and our FIs observations is obtained for an initial $\delta^{13}C_m$ of -0.9 ± 0.3 ‰. Thus, at a depth of 22 km—the estimated entrapment depth for clinopyroxene in sample 14TG12c-b—the solubility model predicts that the melt can retain 1.61 wt% CO_2 (melilitite) and 1.11 wt% (Mg-nephelinite) at saturation, corresponding to a residual fraction (F) of 0.20 at 620 MPa. This suggests that by 22 km depth, the melt would have lost approximately 80 % of its original CO_2 content.

We also explored less probable alternative scenarios, to assess the sensitivity of our model to uncertainties in the assumed CO_2 contents of the parental melts, considering the broader range of OL parental magma formation depths (60–90 km; Ebinger et al., 1997; Mattsson et al., 2013) (Fig. S5A—B). In these scenarios, parental magmas are assumed to form at pressures of 1.6 GPa (~60 km) and 2.5 GPa (~90 km). Following Eguchi and Dasgupta (2018), the corresponding original magmas would contain approximately 4.5–5.5 wt% and 9–10 wt% of dissolved CO_2, respectively (Fig. S5C illustrates the variation in CO_2 solubility with depth for saturated melilititic and Mg-nephelinitic compositions). To reproduce the observed FI $\delta^{13}C$ values under these conditions, the initial $\delta^{13}C_m$ values were estimated as $\delta^{13}C_m(1.6\ GPa) = -1.4 \pm 0.3$ ‰ and $\delta^{13}C_m(2.5\ GPa) = -0.5 \pm 0.3$ ‰. These results indicate that reasonable variations in the assumed CO_2 contents of the parental melt (±2 wt%) or in the magma formation depth (~60–90 km) lead to only minor differences (≤0.5 ‰) in the calculated $\delta^{13}C_m$ values. This modest sensitivity suggests that our main conclusions are not strongly dependent on the exact CO_2 concentration or formation pressure adopted. We further explored an extreme scenario in which the parental magma formed at ~80 km depth contains only 1–2 wt% dissolved CO_2. However, imposing such low initial CO_2 concentrations shifts the modelled degassing trajectories to unrealistically low $\delta^{13}C$ values and fails to reproduce the observed range in our FI data (Fig. S6). Taken together, these tests indicate that the preferred model—assuming parental melts formed at ~75–80 km depth with 7.5–8.6 wt% CO_2—represents the most plausible and internally consistent scenario, providing the best agreement between solubility constraints, melt inclusion data, and measured FI isotopic compositions.

To evaluate the validity of the degassing model starting at 2.2GPa (~80 km), we test whether the pressure-dependent behavior of F (as shown in Fig. 4A) also reproduces the pressure dependence of the $^4He/^{40}Ar^*$ ratio (Fig. 4B). For this, we apply the equations proposed by Macpherson and Mattey (1994) and Hoefs (2009):

$$\frac{He}{Ar}(v) = \frac{He}{Ar}(v,i) * \frac{S_{Ar}}{S_{He}} * F^{\left(\frac{K_{Ar}}{K_{He}} - 1\right)} \quad (6)$$

$$\frac{R_V}{R_{lo}} = F^{\left(\frac{1}{\alpha} - 1\right)} \quad (7)$$

where $^4He/^{40}Ar$ (v) is the ratio in the gas phase for a given residual fraction (F) along the degassing path, and $^4He/^{40}Ar$ (v, *i*) is the ratio at the initial pressure (2.2 GPa); S_{Ar} and S_{He} are the Ar and He solubility constants and considering that no solubility data is available in literature for melilititic nor Mg-nephelinitic magmas, we estimated S_{Ar} and S_{He} assuming a $S_{(He/CO2)} = 1.7$ (also used for the FI data from the 2021 Tajogaite eruption at La Palma; Sandoval-Velasquez et al., 2024) and a $S_{(CO2/Ar)} = 8.5$ (Iacono-Marziano et al., 2010). In the same equations, R_V/R_{lo} is the instantaneous isotope ratio of the vapor leaving the liquid and the remaining liquid and α is the fractionation factor.

The modelled degassing path is shown in Fig. 4B and fits most of the data when the original magma is assumed to have a $^4He/^{40}Ar_{melt}$ ratio of 2.5 and the corresponding vapor phase a $^4He/^{40}Ar_{vap_{ol}}$ ratio of 0.18. Considering that FIs are predominantly secondary in most samples (Fig. S1), we cannot completely rule out that FIs barometry may reflect re-equilibration processes within the OL plumbing system—particularly for sample 14TG21 (clinopyroxene) that presents stretching and necking down patterns (Fig. S1), which clearly deviate from the modelled vapor lines (see dark green square symbol in Fig. 4B). Nonetheless, a positive correlation between FIs barometric data and total gas content (TGC; Fig. S2)—with deeper FIs entrapment estimates associated with higher TGC values—supports the interpretation that barometric estimates are representative of actual FIs trapping pressures (e.g., Boudoire et al., 2018).

In summary, our results and modelling suggest an isotopically heavy carbon signature (potentially −0.9 ‰ for parental magmas forming at 75–80 km depth) for OL primary melts, and by extension, for their mantle source. However, we note that this interpretation is based on a limited dataset of only three samples and therefore requires further testing and validation using a broader set of xenoliths, especially those that preserve deeper entrapment conditions than those recorded in the current study. We also acknowledge that our calculations are based on the assumption that primary melts form at pressures of 2.2 GPa and contain approximately 7.5–8.6 wt% CO_2—an assumption that, while consistent with observations not only at OL but also at other locations such as Hawaii, Texas, Germany, and South Africa (Brey, 1978; Mattsson et al., 2013), still requires additional verification. With these limitations in mind, we emphasize that the decompression-driven degassing of an initial melt with a $\delta^{13}C$ value of ~ − 0.9 ‰ also provides a good

Table 2
Composition of the parental melts considered for the degassing model.

Melt composition	Reference	SiO_2	TiO_2	Al_2O_3	Fe_2O_3	FeO	MgO	CaO	Na_2O	K_2O	P_2O_5
Mg-nephelinite	Mourey et al. (2023)	41,72	4,32	11,5	3,15	12,28	8,15	13	2,63	1,95	0,2
Melilitite	Keller et al. (2006)	38,26	3,79	7,26	–	8,01	15,3	13,44	2,19	1,36	0,89

explanation for the $\delta^{13}C$ vs. $CO_2/^3He$ compositions not only of our FIs samples, but also of OL summit fumaroles and gases from the nearby Rungwe Volcanic Province (Fig. 5; Fischer et al., 2009; Barry et al., 2013).

4.3. Assessing the role of crustal contamination versus mantle metasomatism in controlling $\delta^{13}C$

The possible assimilation of crustal limestones during magma ascent within the OL plumbing system represents an important consideration when evaluating our $\delta^{13}C$ model. However, isotopic constraints from Nd–Sr–Pb systematics and trace-element data strongly argue against any significant crustal contamination of OL primary lavas, carbonatites, or mantle xenoliths. Variations in Nd, Pb, and Sr isotope ratios among OL lavas are best explained by mantle-source heterogeneity—rather than crustal assimilation—involving mixing between HIMU- and EMI-type mantle components (Bell and Simonetti, 1996; Keller et al., 2006; Rooney, 2020). Moreover, mantle xenoliths from nearby cinder cones and tuff deposits, primarily peridotites and pyroxenites, share these isotopic characteristics, confirming derivation from a similarly enriched mantle domain (Cohen et al., 1984; Rudnick et al., 1993; Bell and Simonetti, 1996). This interpretation is further supported by helium-isotope data, which exclude any significant crustal contamination during magma ascent while indicating the involvement of a recycled crustal component within the local SCLM—a feature also recognized in other metasomatized SCLM settings worldwide (Gautheron and Moreira, 2002). In particular, the findings of Mollex et al. (2018) and Mourey et al. (2023)—based on helium-isotope compositions and trace-element characteristics of xenoliths 10TL01, 10TL05, and 14TG21—demonstrate that the ascending magmas did not undergo crustal contamination. Likewise, Keller et al. (2006) showed that OL alkali-rich nephelinites and olivine melilitites, considered potential parental melts for our model, display Ce/Pb, Ce/Y, and Ba/U ratios typical of mantle-derived magmas, thereby excluding a significant crustal contribution.

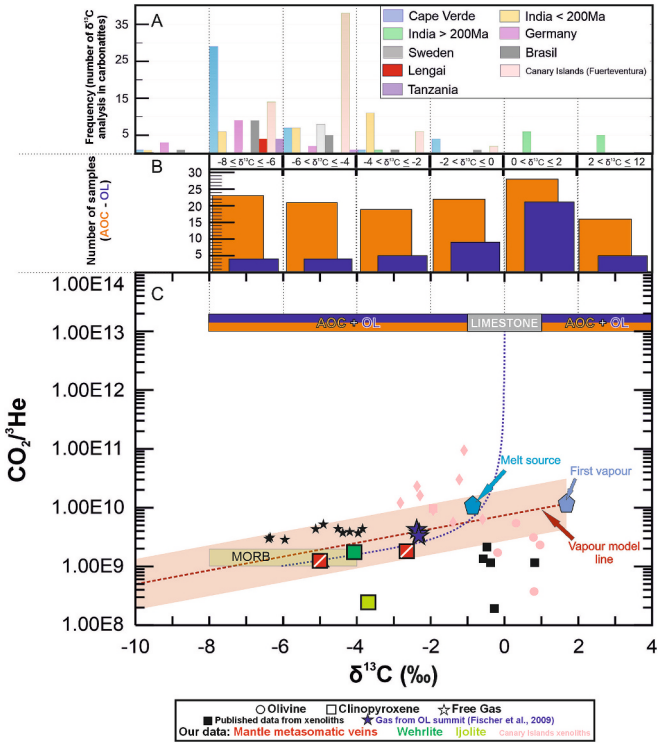

Fig. 5. A) Histogram showing the distribution of $\delta^{13}C$ values from different carbonatites (<180 Ma) around the world (Taylor et al., 1967; Hay and O'Neil, 1983; Keller and Hoefs, 1995; Srivastava and Taylor, 1996; Demény et al., 1998; Mata et al., 2010; Jones et al., 2013; Gales, 2019; Amsellem et al., 2020). B) The histogram shows the number of samples of carbonates hosted in altered oceanic crust – oceanic lithosphere (AOC-OL) reported for each $\delta^{13}C$ class after Li et al. (2019). C) $\delta^{13}C$ vs $CO_2/^3He$. Black symbols representing xenoliths and gas data obtained from volcanoes near OL in Southern Kenya and Tanzania; data is from Halldórsson et al. (2022) and Barry et al. (2013). Canary Islands data is from Sandoval-Velasquez et al. (2021b, 2024). The dotted dark blue line represents a binary mixing curve between two endmembers: Limestone at $\delta^{13}C = 0$ ‰ ($CO_2/^3He = 1.00 \times 10^{13}$) and a MORB-like upper mantle at $\delta^{13}C = -6$ ‰ ($CO_2/^3He = 1.00 \times 10^9$). MORB and limestone $\delta^{13}C$ ranges are designed after Sano and Marty (1995). The dotted red line is the more probable degassing path for the vapor phase fitting our data and the $\delta^{13}C$ of the summit OL fumaroles; the light red area represents the uncertainty of the model based on the maximum and minimum $CO_2/^3He$ of our data and data published in the literature. (For interpretation of the references to colour in this figure legend, the reader is referred to the web version of this article.)

We therefore propose a model (Figs. 4B and 5C) in which a $\delta^{13}C$ of approximately −0.9 ‰ directly reflects the isotopic systematics of a local SCLM infiltrated by carbon-rich metasomatic agents (as observed by Foley and Fischer, 2017; Muirhead et al., 2020). These agents likely carried a recycled crustal (^{13}C-enriched) signature capable of shifting both $\delta^{13}C$ and $CO_2/^3He$ ratios from typical mantle-like values (−8 ‰ to −4 ‰ and ~ 1×10^9, respectively; Sano and Marty, 1995) toward higher ratios (~ − 0.9 ‰ and ~ 1×10^{10}, respectively), approaching the isotopic composition of crustal limestones. This scenario is also consistent with the experiments and isotopic interpretations of Paslick et al. (1995), who attributed Pb-isotope compositions and U/Pb variability in lavas and xenoliths from northern Tanzania (near OL) to partial melting of an ancient, underplated OIB-like component that remained isolated within the lithospheric mantle for approximately 2 Ga. According to those authors, this enriched mantle domain—formed prior to the opening of the East African Rift (~45 Ma; Ebinger et al., 1993; George et al., 1998; Boone et al., 2019; Michon et al., 2022)—originated from the addition of ancient subducted and plume-derived materials to the local SCLM.

We therefore argue that a ^{13}C-rich mantle source likely exists beneath OL, resulting from the infiltration of carbon-bearing metasomatic agents into the local SCLM (Foley and Fischer, 2017; Muirhead et al., 2020) that carried a recycled crustal carbon signature (Figs. 5B and 4C). A comparable process has recently been proposed for both the eastern and western branches of the East African Rift System (Halldórsson et al., 2022) and for several ocean-island settings, including the Canary Islands (Sandoval-Velasquez et al., 2024) and Cape Verde (Lo Forte et al., 2024), where crustal carbon recycling into the mantle is attributed to subducted altered oceanic crust (AOC) or oceanic lithosphere. In the case of OL, the available data do not permit unambiguous discrimination among potential metasomatic sources such as AOC, oceanic lithosphere, or sedimentary carbonates (Fig. 5). Each of these reservoirs could plausibly contribute carbon characterized by relatively heavy $\delta^{13}C$ values and elevated $CO_2/^3He$ ratios. Consequently, our results are best explained by the involvement of a mixed or variably processed recycled-carbon component, rather than by a single, compositionally uniform source.

4.4. Implications for the origin of OL carbonatites

Existing models for the generation of carbonatitic magmas fall into two contrasting categories (Wallace and Green, 1988; Peterson, 1989; Dawson et al., 1995; Fischer et al., 2009; Hammouda et al., 2014). According to one view (Wallace and Green, 1988; Hammouda et al., 2014), carbonatites form in the mantle during partial melting of carbon-enriched mantle lithologies. In contrast, alternative models (Peterson, 1989; Fischer et al., 2009; Mourey et al., 2023) propose that carbonatites originate through low-degree partial melting of a C-poor mantle followed by extreme differentiation of, and immiscibility from, the corresponding alkaline silicate melt precursor. At OL, petrological and volatile geochemical evidence supports the idea that immiscibility

between peralkaline nephelinitic melts and natrocarbonatites occurs at shallow crustal depths (<300 MPa), and represents the most plausible mechanism for generating the erupted carbonatites (Kjarsgaard et al., 1995; Fischer et al., 2009; Mollex et al., 2018; France et al., 2022).

Globally, carbon isotopes in relatively young (<180 Ma) carbonatites (Fig. 5A) are predominantly characterized by negative $\delta^{13}C$ values (< −4 ‰), within the typical MORB mantle range. At OL, fresh natrocarbonatites erupted between 1995 and 2007 exhibit $\delta^{13}C$ values between −6.3 ‰ and − 7.8 ‰ (Keller and Hoefs, 1995; Amsellem et al., 2020). These values, together with noble gas data, have been interpreted as evidence for a MORB-like mantle source beneath OL (Fischer et al., 2009). However, if carbonatites at OL are generated by shallow-level immiscibility from an alkaline nephelinitic melt, their carbon isotope composition may not directly reflect the isotopic signature of the mantle source. Our model (Fig. 4A) shows that at ~270 MPa (~10 km depth), corresponding to the upper pressure limit for immiscibility, a silicate melt could have already lost up to ~93 % of its original carbon through degassing. As a result, the residual carbon—and thus the carbonatite derived from it—would exhibit a $\delta^{13}C$ value several per mil lighter than that of the source melt. The degassing-driven $\delta^{13}C$ depletion in carbonatites is further supported by Figs. 4A and 5C, where the $\delta^{13}C$ values of carbonatites are more negative than even the most ^{13}C-depleted FIs samples in our dataset.

We conclude that the low $\delta^{13}C$ values observed in OL carbonatites are best explained by isotopic fractionation during magmatic degassing, rather than by a MORB-type mantle source. According to our model results (Fig. 4A), the isotopic composition of carbonatites is consistent with that of a late-stage, carbon-depleted melt formed at pressures of 270–320 MPa (10–12 km depth) within the mid-crustal magma reservoir (at ~8–12 km depth; Roecker et al., 2017; Reiss et al., 2022; Daud et al., 2023), yielding residual $\delta^{13}C$ values between −6 ‰ and − 8 ‰.

5. Conclusions

We report the first combined carbon and noble gas (He—Ar) isotopic characterization of FIs hosted in cumulates (ijolites, wehrlites) and mantle xenoliths (harzburgites and lherzolites) from the Oldoinyo Lengai (OL) volcano. Using Raman spectroscopy, we infer FI entrapment pressures of 33–261 MPa (1–4 km depth) for shallow cumulates (ijolites), 1–498 MPa (0–19 km) for deeper cumulates (wehrlites), and 39–670 MPa (1–25 km) for mantle xenoliths. These pressure/depth ranges fall entirely within the transcrustal magma plumbing system of OL, suggesting that FIs were either reset (re-equilibrated) during xenolith transport through crustal storage zones or that they were directly trapped at these crustal depths, rather than in the mantle. Moreover, positive correlations between total gas content and barometric data from FIs suggest that barometry might reflects actual fluid trapping pressures, rather than re-equilibration processes within the OL plumbing system—particularly in the case of lherzolites and ijolites, which align with modelled $\delta^{13}C$ and $^{4}He/^{40}Ar^{*}$ degassing trends.

CO_2 in FIs exhibits $\delta^{13}C$ values between −5.0 ‰ and − 2.7 ‰, overlapping with those reported for OL fumaroles. The heaviest carbon isotope compositions correspond to the highest entrapment pressures/depths (670 MPa, or 25 km), and, when considered alongside the observed positive pressure dependence of the $^{4}He/^{40}Ar^{*}$ ratio, indicate that FIs isotopic and chemical compositions are controlled by fractional (open-system) magmatic degassing during magma ascent and decompression. We therefore develop a pressure-dependent open-system degassing model, assuming a starting condition of a primary melilitic/Mg-nephelinitic melt formed at 75–80 km depth, containing ~7.5–8.6 wt% CO_2. Comparison between the model and FIs compositions requires that the parental melt had a relatively heavy isotopic signature, with a $\delta^{13}C$ of −0.90 ± 0.30 ‰. This heavy $\delta^{13}C$ value suggests that OL magmatism originates from a mantle domain enriched in carbon through metasomatic agents bearing a crustal carbon signature. In light of this model, the light carbon isotopic composition of OL carbonatites ($\delta^{13}C$ = −6.3 ‰ to −7.8 ‰) supports models in which carbonatites form via immiscibility from an alkali-rich, ultramafic silicate melt precursor at shallow crustal levels (10-12 km depth).

Finally, the lower-than-MORB helium isotope compositions observed in FIs—averaging 6.63 ± 0.39 Ra in mantle xenoliths and 6.24 ± 0.50 Ra in crustal cumulates—are consistent with the enriched nature of the SCLM underlying OL.

CRediT authorship contribution statement

A. Sandoval-Velasquez: Writing – original draft, Investigation, Formal analysis, Data curation, Conceptualization, Visualization. **J. Lages:** Resources, Investigation, Data curation, Conceptualization. **G. Boudoire:** Writing – review & editing, Resources, Investigation, Funding acquisition, Conceptualization. **A. Aiuppa:** Writing – review & editing, Resources, Project administration, Funding acquisition, Conceptualization. **F.M. Lo Forte:** Investigation, Formal analysis, Data curation. **L. France:** Writing – review & editing, Supervision, Resources, Funding acquisition, Data curation. **A.L. Rizzo:** Writing – review & editing, Visualization, Investigation, Formal analysis, Conceptualization.

Declaration of competing interest

The authors declare that they have no known competing financial interests or personal relationships that could have appeared to influence the work reported in this paper.

Acknowledgements

We thank Mariano Tantillo and Mariagrazia Misseri for helping in samples preparation and CO_2 extraction from minerals, and Igor Oliveri and Giorgio Capasso for the isotope analysis of carbon of CO_2 performed in the stable isotope laboratory of INGV-Palermo. This research was funded by the Italian Minister (PRIN2017LMNLAW and PRIN2022-HA8XCS), by the Deep Carbon Observatory, by the RETURN Extended Partnership funded by the European Union Next-Generation EU (National Recovery and Resilience Plan–NRRP, Mission 4, Component 2, Investment 1.3–D.D. 1243 2/8/2022, PE0000005), by the National Biodiversity Future Center (National Recovery and Resilience Plan–NRRP, Mission 4, Component 2, Investment 1.4, CN00000033). This work has been also supported by the French National Research Agency through the national program 'Investissements d'avenir' with the reference ANR-10-LABX-21-01/LABEX RESSOURCES21 and through the project GECO-REE (ANR-16-CE01-0003-01) to LF. LF also thanks the Tanzania Commission for Science and Technology (COSTECH) for field permits and Emmanuel Kazimoto from Dar Es Salaam University for assistance during field work. Finally, we are very grateful to the-Editor in Chief Prof. Don Porcelli and two anonymous Reviewers whose comments and suggestions improved our manuscript.

Appendix A. Supplementary data

Supplementary data to this article can be found online at https://doi.org/10.1016/j.chemgeo.2025.123126.

Data availability

Data will be made available on request.

References

Aiuppa, A., Bitetto, M., Delle Donne, D., La Monica, F.P., Tamburello, G., Coppola, D., Della Schiava, M., Innocenti, L., Lacanna, G., Laiolo, M., Massimetti, F., Pistolesi, M., Silengo, M.C., Ripepe, M., 2021. Volcanic CO_2 tracks the incubation period of basaltic paroxysms. Sci. Adv. 7, eabh0191. https://doi.org/10.1126/sciadv.abh0191.

Amsellem, E., Moynier, F., Bertrand, H., Bouyon, A., Mata, J., Tappe, S., Day, J.M.D., 2020. Calcium isotopic evidence for the mantle sources of carbonatites. Sci. Adv. 6, eaba3269. https://doi.org/10.1126/sciadv.aba3269.

Aubaud, C., 2022. Carbon stable isotope constraints on CO2 degassing models of ridge, hotspot and arc magmas. Chem. Geol. 605, 120962. https://doi.org/10.1016/j.chemgeo.2022.120962.

Barry, P.H., Hilton, D.R., Fischer, T.P., de Moor, J.M., Mangasini, F., Ramirez, C., 2013. Helium and carbon isotope systematics of cold "mazuku" CO2 vents and hydrothermal gases and fluids from Rungwe Volcanic Province, southern Tanzania. Chem. Geol. 339, 141–156. https://doi.org/10.1016/j.chemgeo.2012.07.003.

Bell, K., Dawson, J.B., 1995. Nd and Sr isotope systematics of the active carbonatite Volcano, Oldoinyo Lengai. In: Bell, Keith, Keller, J. (Eds.), Carbonatite Volcanism, IAVCEI Proceedings in Volcanology. Springer Berlin Heidelberg, Berlin, Heidelberg, pp. 100–112. https://doi.org/10.1007/978-3-642-79182-6_8.

Carbonatite volcanism: Oldoinyo Lengai and the petrogenesis of natrocarbonatites. In: Bell, K., Keller, J. (Eds.), 1995. IAVCEI Proceedings in Volcanology. Springer Berlin Heidelberg, Berlin, Heidelberg. https://doi.org/10.1007/978-3-642-79182-6.

Bell, K., Simonetti, A., 1996. Carbonatite magmatism and plume activity: Implications from the Nd, Pb and Sr isotope systematics of Oldoinyo Lengai. J. Petrol. 37, 1321–1339. https://doi.org/10.1093/petrology/37.6.1321.

Boone, S.C., Kohn, B.P., Gleadow, A.J.W., Morley, C.K., Seiler, C., Foster, D.A., 2019. Birth of the East African Rift System: Nucleation of magmatism and strain in the Turkana Depression. Geology 47, 886–890. https://doi.org/10.1130/G46468.1.

Boudoire, G., Rizzo, A.L., Di Muro, A., Grassa, F., Liuzzo, M., 2018. Extensive CO2 degassing in the upper mantle beneath oceanic basaltic volcanoes: first insights from Piton de la Fournaise volcano (La Réunion Island). Geochim. Cosmochim. Acta 235, 376–401. https://doi.org/10.1016/j.gca.2018.06.004.

Boudoire, G., Brugier, Y.-A., Di Muro, A., Wörner, G., Arienzo, I., Metrich, N., Zanon, V., Braukmüller, N., Kronz, A., Le Moigne, Y., Michon, L., 2019. Eruptive activity on the Western Flank of Piton de la Fournaise (La Réunion Island, Indian Ocean): Insights on Magma transfer, Storage and Evolution at an Oceanic Volcanic Island. J. Petrol. 60, 1717–1752. https://doi.org/10.1093/petrology/egz045.

Brey, G., 1978. Origin of olivine melilitites — chemical and experimental constraints. J. Volcanol. Geotherm. Res. 3, 61–88. https://doi.org/10.1016/0377-0273(78)90004-5.

Brune, S., Williams, S.E., Müller, R.D., 2017. Potential links between continental rifting, CO2 degassing and climate change through time. Nat. Geosci. 10, 941–946. https://doi.org/10.1038/s41561-017-0003-6.

Casola, V., France, L., Galy, A., Bouden, N., Villeneuve, J., 2020. No evidence for carbon enrichment in the mantle source of carbonatites in eastern Africa. Geology 48, 971–975. https://doi.org/10.1130/G47629.1.

Christensen, N.I., Mooney, W.D., 1995. Seismic velocity structure and composition of the continental crust: a global view. J. Geophys. Res. Solid Earth 100, 9761–9788. https://doi.org/10.1029/95JB00259.

Cohen, R.S., O'Nions, R.K., Dawson, J.B., 1984. Isotope geochemistry of xenoliths from East Africa: Implications for development of mantle reservoirs and their interaction. Earth Planet. Sci. Lett. 68, 209–220. https://doi.org/10.1016/0012-821X(84)90153-5.

Daud, N., Stamps, D.S., Battaglia, M., Huang, M.-H., Saria, E., Ji, K.-H., 2023. Elucidating the magma plumbing system of Ol Doinyo Lengai (Natron Rift, Tanzania) using satellite geodesy and numerical modeling. J. Volcanol. Geotherm. Res. 438, 107821. https://doi.org/10.1016/j.jvolgeores.2023.107821.

Dawson, J.B., 1962. The geology of Oldoinyo Lengai. Bull. Volcanol. 24, 349–387. https://doi.org/10.1007/BF02599356.

Dawson, J.B., Pinkerton, H., Norton, G.E., Pyle, D.M., Browning, P., Jackson, D., Fallick, A.E., 1995. Petrology and geochemistry of Oldoinyo Lengai Lavas Extruded in November 1988: magma source, ascent and crystallization. In: Bell, K., Keller, J. (Eds.), Carbonatite Volcanism, IAVCEI Proceedings in Volcanology. Springer Berlin Heidelberg, Berlin, Heidelberg, pp. 47–69. https://doi.org/10.1007/978-3-642-79182-6_5.

De Moor, J.M., Fischer, T.P., King, P.L., Botcharnikov, R.E., Hervig, R.L., Hilton, D.R., Barry, P.H., Mangasini, F., Ramirez, C., 2013. Volatile-rich silicate melts from Oldoinyo Lengai volcano (Tanzania): Implications for carbonatite genesis and eruptive behavior. Earth Planet. Sci. Lett. 361, 379–390. https://doi.org/10.1016/j.epsl.2012.11.006.

Deines, P., 2002. The carbon isotope geochemistry of mantle xenoliths. Earth Sci. Rev. 58, 247–278. https://doi.org/10.1016/S0012-8252(02)00064-8.

Demény, A., Ahijado, A., Casillas, R., Vennemann, T.W., 1998. Crustal contamination and fluid/rock interaction in the carbonatites of Fuerteventura (Canary Islands, Spain): a C, O, H isotope study. Lithos 44, 101–115. https://doi.org/10.1016/S0024-4937(98)00050-4.

Ebinger, C.J., Yemane, T., Woldegabriel, G., Aronson, J.L., Walter, R.C., 1993. Late Eocene–Recent volcanism and faulting in the southern main Ethiopian rift. J. Geol. Soc. Lond. 150, 99–108. https://doi.org/10.1144/gsjgs.150.1.0099.

Ebinger, C., Djomani, Y.P., Mbede, E., Foster, A., Dawson, J.B., 1997. Rifting Archaean lithosphere: the Eyasi-Manyara-Natron rifts, East Africa. J. Geol. Soc. Lond. 154, 947–960. https://doi.org/10.1144/gsjgs.154.6.0947.

Eguchi, J., Dasgupta, R., 2018. A CO2 solubility model for silicate melts from fluid saturation to graphite or diamond saturation. Chem. Geol. 487, 23–38. https://doi.org/10.1016/j.chemgeo.2018.04.012.

Fischer, T.P., Takahata, N., Sano, Y., Sumino, H., Hilton, D.R., 2005. Nitrogen isotopes of the mantle: Insights from mineral separates. Geophys. Res. Lett. 32, 2005GL022792. https://doi.org/10.1029/2005GL022792.

Fischer, T.P., Burnard, P., Marty, B., Hilton, D.R., Füri, E., Palhol, F., Sharp, Z.D., Mangasini, F., 2009. Upper-mantle volatile chemistry at Oldoinyo Lengai volcano and the origin of carbonatites. Nature 459, 77–80. https://doi.org/10.1038/nature07977.

Foley, S.F., Fischer, T.P., 2017. An essential role for continental rifts and lithosphere in the deep carbon cycle. Nat. Geosci. 10, 897–902. https://doi.org/10.1038/s41561-017-0002-7.

Foley, S.F., Link, K., Tiberindwa, J.V., Barifaijo, E., 2012. Patterns and origin of igneous activity around the Tanzanian craton. J. Afr. Earth Sci. 62, 1–18. https://doi.org/10.1016/j.jafrearsci.2011.10.001.

France, L., Brouillet, F., Lang, S., 2022. Early carbonatite magmatism at Oldoinyo Lengai volcano (Tanzania): carbonatite–silicate melt immiscibility in Lengai I melt inclusions. Comptes Rendus Géoscience 353, 273–288. https://doi.org/10.5802/crgeos.99.

Frezzotti, M.-L., Touret, J.L.R., Neumann, E.-R., 2002. Ephemeral carbonate melts in the upper mantle: carbonate-silicate immiscibility in microveins and inclusions within spinel peridotite xenoliths, La Gomera, Canary Islands. Eur. J. Mineral. 14, 891–904. https://doi.org/10.1127/0935-1221/2002/0014-0891.

Gales, E., 2019. Carbonatites as a Record of the Carbon Isotope Composition of Large Igneous Province Outgassing. City University of New York, New York.

Gautheron, C., Moreira, M., 2002. Helium signature of the subcontinental lithospheric mantle. Earth Planet. Sci. Lett. 199, 39–47. https://doi.org/10.1016/S0012-821X(02)00563-0.

Gennaro, M.E., Grassa, F., Martelli, M., Renzulli, A., Rizzo, A.L., 2017. Carbon isotope composition of CO 2 -rich inclusions in cumulate-forming mantle minerals from Stromboli volcano (Italy). J. Volcanol. Geotherm. Res. 346, 95–103. https://doi.org/10.1016/j.jvolgeores.2017.04.001.

George, R., Rogers, N., Kelley, S., 1998. Earliest magmatism in Ethiopia: evidence for two mantle plumes in one flood basalt province. Geology 26, 923. https://doi.org/10.1130/0091-7613(1998)026<0923:EMIEEF>2.3.CO;2.

Graham, D.W., 2002. Noble gas isotope geochemistry of mid-ocean ridge and Ocean Island Basalts: characterization of mantle source reservoirs. Rev. Mineral. Geochem. 47, 247–317. https://doi.org/10.2138/rmg.2002.47.8.

Halldórsson, S.A., Hilton, D.R., Marshall, E.W., Ranta, E., Ingvason, A., Chakraborty, S., Robin, J.G., Rasmussen, M.B., Gibson, S.A., Ono, S., Scarsi, P., Abebe, T., Hopp, J., Barry, P.H., Castillo, P.R., 2022. Evidence from gas-rich ultramafic xenoliths for Superplume-derived recycled volatiles in the East African sub-continental mantle. Chem. Geol. 589, 120682. https://doi.org/10.1016/j.chemgeo.2021.120682.

Hammouda, T., Chantel, J., Manthilake, G., Guignard, J., Crichton, W., 2014. Hot mantle geotherms stabilize calcic carbonatite magmas up to the surface. Geology 42, 911–914. https://doi.org/10.1130/G35778.1.

Hay, R.L., O'Neil, J.R., 1983. Carbonatite tuffs in the Laetolil Beds of Tanzania and the Kaiserstuhl in Germany. Contrib. Mineral. Petrol. 82, 403–406. https://doi.org/10.1007/BF00399717.

Hilton, D.R., Halldórsson, S.A., Barry, P.H., Fischer, T.P., De Moor, J.M., Ramirez, C.J., Mangasini, F., Scarsi, P., 2011. Helium isotopes at Rungwe Volcanic Province, Tanzania, and the origin of East African Plateaux: HIGH HELIUM ISOTOPE RATIOS AT RUNGWE. Geophys. Res. Lett. 38. https://doi.org/10.1029/2011GL049589 n/a-n/a.

Hoefs, J., 2009. Stable Isotope Geochemistry. Springer Berlin Heidelberg, Berlin, Heidelberg. https://doi.org/10.1007/978-3-540-70708-0.

Iacono-Marziano, G., Paonita, A., Rizzo, A., Scaillet, B., Gaillard, F., 2010. Noble gas solubilities in silicate melts: New experimental results and a comprehensive model of the effects of liquid composition, temperature and pressure. Chem. Geol. 279, 145–157. https://doi.org/10.1016/j.chemgeo.2010.10.017.

Javoy, M., Pineau, F., Agrinier, P., 1989. Volatiles and stable isotopes in recycling. In: Hart, S.R., Gülen, L. (Eds.), Crust/Mantle Recycling at Convergence Zones. Springer Netherlands, Dordrecht, pp. 121–138. https://doi.org/10.1007/978-94-009-0895-6_13.

Jones, A.P., Genge, M., Carmody, L., 2013. Carbonate melts and carbonatites. Rev. Mineral. Geochem. 75, 289–322. https://doi.org/10.2138/rmg.2013.75.10.

Keller, J., Hoefs, J., 1995. Stable isotope characteristics of recent natrocarbonatites from Oldoinyo Lengai. In: Bell, K., Keller, Jörg (Eds.), Carbonatite Volcanism, IAVCEI Proceedings in Volcanology. Springer Berlin Heidelberg, Berlin, Heidelberg, pp. 113–123. https://doi.org/10.1007/978-3-642-79182-6_9.

Keller, J., Zaitsev, A., Wiedenmann, D., 2006. Primary magmas at Oldoinyo Lengai: the role of olivine melilitites. Lithos 91, 150–172. https://doi.org/10.1016/j.lithos.2006.03.014.

Kjarsgaard, B.A., Hamilton, D.L., Peterson, T.D., 1995. Peralkaline Nephelinite/Carbonatite Liquid Immiscibility: Comparison of phase Compositions in experiments and Natural Lavas from Oldoinyo Lengai. In: Bell, K., Keller, J. (Eds.), Carbonatite Volcanism, IAVCEI Proceedings in Volcanology. Springer Berlin Heidelberg, Berlin, Heidelberg, pp. 163–190. https://doi.org/10.1007/978-3-642-79182-6_13.

Koepenick, K.W., Brantley, S.L., Thompson, J.M., Rowe, G.L., Nyblade, A.A., Moshy, C., 1996. Volatile emissions from the crater and flank of Oldoinyo Lengai volcano, Tanzania. J. Geophys. Res. Solid Earth 101, 13819–13830. https://doi.org/10.1029/96JB00173.

Li, K., Li, L., Pearson, D.G., Stachel, T., 2019. Diamond isotope compositions indicate altered igneous oceanic crust dominates deep carbon recycling. Earth Planet. Sci. Lett. 516, 190–201. https://doi.org/10.1016/j.epsl.2019.03.041.

Lo Forte, F.M., Boudoire, G., Frezzotti, M.L., Rotolo, S.G., Sandoval-Velasquez, A., Viveiros, F., Zanon, V., Aiuppa, A., Rizzo, A.L., 2024. The helium and carbon isotopic signature of Ocean island basalts: Insights from Fogo volcano (Cape Verde archipelago). Earth Planet. Sci. Lett. 645, 118930. https://doi.org/10.1016/j.epsl.2024.118930.

Macpherson, C., Mattey, D., 1994. Carbon isotope variations of CO2 in Central Lau Basin basalts and ferrobasalts. Earth Planet. Sci. Lett. 121, 263–276. https://doi.org/10.1016/0012-821X(94)90072-8.

Mata, J., Moreira, M., Doucelance, R., Ader, M., Silva, L.C., 2010. Noble gas and carbon isotopic signatures of Cape Verde oceanic carbonatites: Implications for carbon provenance. Earth Planet. Sci. Lett. 291, 70–83. https://doi.org/10.1016/j.epsl.2009.12.052.

Mattey, D.P., 1991. Carbon dioxide solubility and carbon isotope fractionation in basaltic melt. Geochim. Cosmochim. Acta 55, 3467–3473. https://doi.org/10.1016/0016-7037(91)90508-3.

Mattsson, H.B., Nandedkar, R.H., Ulmer, P., 2013. Petrogenesis of the melilititic and nephelinitic rock suites in the Lake Natron–Engaruka monogenetic volcanic field, northern Tanzania. Lithos 179, 175–192. https://doi.org/10.1016/j.lithos.2013.07.012.

Michon, L., Famin, V., Quidelleur, X., 2022. Evolution of the East African Rift System from trap-scale to plate-scale rifting. Earth Sci. Rev. 231, 104089. https://doi.org/10.1016/j.earscirev.2022.104089.

Mollex, G., Füri, E., Burnard, P., Zimmermann, L., Chazot, G., Kazimoto, E.O., Marty, B., France, L., 2018. Tracing helium isotope compositions from mantle source to fumaroles at Oldoinyo Lengai volcano, Tanzania. Chem. Geol. 480, 66–74. https://doi.org/10.1016/j.chemgeo.2017.08.015.

Mourey, A.J., France, L., Ildefonse, B., Gurenko, A., Laporte, D., 2023. Genesis of carbonatite at Oldoinyo Lengai (Tanzania) from Olivine Nephelinite: protracted melt evolution and reactive porous flow in deep crustal mushes. J. Petrol. 64, egad084. https://doi.org/10.1093/petrology/egad084.

Muirhead, J.D., Fischer, T.P., Oliva, S.J., Laizer, A., Van Wijk, J., Currie, C.A., Lee, H., Judd, E.J., Kazimoto, E., Sano, Y., Takahata, N., Tiberi, C., Foley, S.F., Dufek, J., Reiss, M.C., Ebinger, C.J., 2020. Displaced cratonic mantle concentrates deep carbon during continental rifting. Nature 582, 67–72. https://doi.org/10.1038/s41586-020-2328-3.

Paslick, C., Halliday, A., James, D., Dawson, J.B., 1995. Enrichment of the continental lithosphere by OIB melts: Isotopic evidence from the volcanic province of northern Tanzania. Earth Planet. Sci. Lett. 130, 109–126. https://doi.org/10.1016/0012-821X(95)00002-T.

Pearson, D.G., Canil, D., Shirey, S.B., 2014. Mantle samples included in volcanic rocks. In: Treatise on Geochemistry. Elsevier, pp. 169–253. https://doi.org/10.1016/B978-0-08-095975-7.00216-3.

Peterson, T.D., 1989. Peralkaline nephelinites: II. Low pressure fractionation and the hypersodic lavas of Oldoinyo L'engai. Contrib. Mineral. Petrol. 102, 336–346. https://doi.org/10.1007/BF00373727.

Plasman, M., Tiberi, C., Ebinger, C., Gautier, S., Albaric, J., Peyrat, S., Déverchère, J., Le Gall, B., Tarits, P., Roecker, S., Wambura, F., Muzuka, A., Mulibo, G., Mtelela, K., Msabi, M., Kianji, G., Hautot, S., Perrot, J., Gama, R., 2017. Lithospheric low-velocity zones associated with a magmatic segment of the Tanzanian Rift, East Africa. Geophys. J. Int. 210, 465–481. https://doi.org/10.1093/gji/ggx177.

Reiss, M.C., Muirhead, J.D., Laizer, A.S., Link, F., Kazimoto, E.O., Ebinger, C.J., Rümpker, G., 2021. The Impact of complex Volcanic Plumbing on the Nature of Seismicity in the developing Magmatic Natron Rift, Tanzania. Front. Earth Sci. 8, 609805. https://doi.org/10.3389/feart.2020.609805.

Reiss, M.C., De Siena, L., Muirhead, J.D., 2022. The interconnected magmatic plumbing system of the Natron Rift. Geophys. Res. Lett. 49. https://doi.org/10.1029/2022GL098922 e2022GL098922.

Rizzo, A.L., Pelorosso, B., Coltorti, M., Ntaflos, T., Bonadiman, C., Matusiak-Małek, M., Italiano, F., Bergonzoni, G., 2018. Geochemistry of Noble gases and CO2 in Fluid Inclusions from Lithospheric Mantle beneath Wilcza Góra (lower Silesia, Southwest Poland). Front. Earth Sci. 6, 215. https://doi.org/10.3389/feart.2018.00215.

Roecker, S., Ebinger, C., Tiberi, C., Mulibo, G., Ferdinand-Wambura, R., Mtelela, K., Kianji, G., Muzuka, A., Gautier, S., Albaric, J., Peyrat, S., 2017. Subsurface images of the Eastern Rift, Africa, from the joint inversion of body waves, surface waves and gravity: investigating the role of fluids in early-stage continental rifting. Geophys. J. Int. 210, 931–950. https://doi.org/10.1093/gji/ggx220.

Roedder, E., 1984. Fluid Inclusions: An Introduction to Studies of all Types of Fluid Inclusions, Gas, Liquid, or Melt, Trapped in Materials from Earth and Space, and their Application to the Understanding of Geologic Processes. Mineralogical Society of America.

Rooney, T.O., 2020. The Cenozoic magmatism of East Africa: Part V – Magma sources and processes in the East African Rift. Lithos 360–361, 105296. https://doi.org/10.1016/j.lithos.2019.105296.

Rudnick, R.L., McDonough, W.F., Chappell, B.W., 1993. Carbonatite metasomatism in the northern Tanzanian mantle: Petrographic and geochemical characteristics. Earth Planet. Sci. Lett. 114, 463–475. https://doi.org/10.1016/0012-821X(93)90076-L.

Sandoval-Velasquez, A., Rizzo, A.L., Frezzotti, M.L., Saucedo, R., Aiuppa, A., 2021a. The composition of fluids stored in the central Mexican lithospheric mantle: Inferences from noble gases and CO2 in mantle xenoliths. Chem. Geol. 576, 120270. https://doi.org/10.1016/j.chemgeo.2021.120270.

Sandoval-Velasquez, A., Rizzo, A.L., Aiuppa, A., Remigi, S., Padrón, E., Pérez, N.M., Frezzotti, M.L., 2021b. Recycled crustal carbon in the depleted mantle source of El Hierro volcano, Canary Islands. Lithos 400–401, 106414. https://doi.org/10.1016/j.lithos.2021.106414.

Sandoval-Velasquez, A., Casetta, F., Ntaflos, T., Aiuppa, A., Coltorti, M., Frezzotti, M.L., Alonso, M., Padrón, E., Pankhurst, M., Pérez, N.M., Rizzo, A.L., 2024. 2021 Tajogaite eruption records infiltration of crustal fluids within the upper mantle beneath La Palma, Canary Islands. Front. Earth Sci. 12, 1303872. https://doi.org/10.3389/feart.2024.1303872.

Sano, Y., Marty, B., 1995. Origin of carbon in fumarolic gas from island arcs. Chem. Geol. 119, 265–274. https://doi.org/10.1016/0009-2541(94)00097-R.

Schmidt, M.W., Giuliani, A., Poli, S., 2024. The Origin of Carbonatites—Combining the Rock Record with Available Experimental Constraints. J. Petrol. 65, egae105. https://doi.org/10.1093/petrology/egae105.

Sherrod, D.R., Magigita, M.M., Kwelwa, S., 2013. Geologic Map of Oldonyo Lengai (Oldoinyo Lengai) and Surroundings, Arusha Region, United Republic of Tanzania.

Srivastava, R.K., Taylor, L.A., 1996. Carbon- and oxygen-isotope variations in Indian carbonatites. Int. Geol. Rev. 38, 419–429. https://doi.org/10.1080/00206819709465344.

Taylor, H.P., Frechen, J., Degens, E.T., 1967. Oxygen and carbon isotope studies of carbonatites from the Laacher See District, West Germany and the Alnö District, Sweden. Geochim. Cosmochim. Acta 31, 407–430. https://doi.org/10.1016/0016-7037(67)90051-8.

Teague, A.J., Seward, T.M., Harrison, D., 2008. Mantle source for Oldoinyo Lengai carbonatites: evidence from helium isotopes in fumarole gases. J. Volcanol. Geotherm. Res. 175, 386–390. https://doi.org/10.1016/j.jvolgeores.2008.04.001.

Wallace, M.E., Green, D.H., 1988. An experimental determination of primary carbonatite magma composition. Nature 335, 343–346. https://doi.org/10.1038/335343a0.

Yaxley, G.M., Anenburg, M., Tappe, S., Decree, S., Guzmics, T., 2022. Carbonatites: Classification, sources, Evolution, and Emplacement. Annu. Rev. Earth Planet. Sci. 50, 261–293. https://doi.org/10.1146/annurev-earth-032320-104243.